HHS Public Access

Author manuscript

*ACS Nano*. Author manuscript; available in PMC 2021 January 28.

Published in final edited form as:

*ACS Nano*. 2020 January 28; 14(1): 142–152. doi:10.1021/acsnano.9b05660.

# Use of Oppositely-Polarized External Magnets to Improve the Accumulation and Penetration of Magnetic Nanocarriers into Solid Tumors

**Jessica F. Liu**[†], **Ziyang Lan**[†], **Carolina Ferrari**[†], **Joel M. Stein**[‡], **Elizabeth Higbee-Dempsey**[†,§], **Lesan Yan**[†], **Ahmad Amirshaghaghi**[†], **Zhiliang Cheng**[†], **David Issadore**[#†,*], **Andrew Tsourkas**[#†,*]

[†]Department of Bioengineering, School of Engineering and Applied Sciences, University of Pennsylvania, Philadelphia, Pennsylvania 19104, United States

[‡]Department of Radiology, Division of Neuroradiology, Hospital of the University of Pennsylvania, Philadelphia, Pennsylvania 19104, United States

[§]Biochemistry and Molecular Biophysics Graduate Group, Perelman School of Medicine, University of Pennsylvania, Philadelphia, Pennsylvania 19104, United States

[#] These authors contributed equally to this work.

## Abstract

Drug delivery to solid tumors is hindered by hydrostatic and physical barriers that limit the penetration of nanocarriers into tumor tissue. When exploiting the enhanced permeability and retention (EPR) effect for passive targeting of nanocarriers, the increased interstitial fluid pressure and dense extracellular matrix in tumors limits the distribution of the nanocarriers to perivascular regions. Previous strategies have shown that magnetophoresis enhances accumulation and penetration of nanoparticles into solid tumors. However, because magnetic fields fall off rapidly with distance from the magnet, these methods have been limited to use in superficial tumors. To overcome this problem, we have developed a system comprising two oppositely-polarized magnets that enables the penetration of magnetic nanocarriers into more deeply-seeded tumors. Using this method, we demonstrate a 5-fold increase in the penetration and a 3-fold increase in the accumulation of magnetic nanoparticles within solid tumors compared to EPR.

### Keywords

magnetophoresis; tumor; magnetic; nanoparticles; penetration

[*]Corresponding Author: Andrew Tsourkas, Department of Bioengineering, School of Engineering and Applied Sciences, University of Pennsylvania, 210 S. 33rd St. Philadelphia, PA 19104, United States. atsourk@seas.upenn.edu, David Issadore, Department of Bioengineering, School of Engineering and Applied Sciences, University of Pennsylvania, 210 S. 33rd St. Philadelphia, PA 19104, United States. issadore@seas.upenn.edu.

Author Contributions

The manuscript was written through contributions of all authors. All authors have given approval to the final version of the manuscript.

**Supporting Information Available:** Supplemental figures (PDF) containing further nanoparticle characterization, detailed device design and characterization, and additional MRI data. This material is available free of charge *via* the Internet at http://pubs.acs.org.

Nanocarriers have emerged as a promising new platform for imaging and therapeutic applications. They are able to carry high payloads, reduce off-target toxicity of cargo, and have the potential to more effectively deliver cargo to target cells. However, poor tumor penetration can severely limit the efficacy of nanocarriers within solid tumors, which account for > 80% of all cancer types.[1] Selective accumulation of nanoparticles in solid tumors generally relies on the enhanced permeability and retention (EPR) effect, a form of passive targeting that takes advantage of the abnormal anatomy and physiology of tumors (*i.e.* leaky vasculature, endothelial fenestrations, and poor lymphatic drainage).[2,3] Unfortunately, with EPR, diffusion within the tumor interstitium is slow and nanocarriers often do not move far beyond the vessel wall.[4,5] This limitation is primarily due to the increased interstitial fluid pressure (IFP) and the dense extracellular matrix (ECM) in tumor tissues.[6,7] While the IFP in normal tissues is typically between 1–3 mmHg, the IFP of tumors can be as high as 10–30 mmHg.[8] Therefore, although the pore size of the extracellular matrix (ECM) in tumors has been reported to be hundreds of nanometers,[6,9] convective flow from the vasculature into the interstitial tissue is limited.[2] Accordingly, nanoparticle penetration into tumors is primarily determined by the rate of particle diffusion,[2] and transport of nanocarriers into tumor tissues is often restricted to perivascular regions.[7,10,11] Various groups have found that in the absence of convective flow, larger nanoparticles, which may carry larger payloads, travel significantly slower through the ECM.[4,12] This has significant implications for tumor therapy: for example, Wang *et al.* found that due to poor tissue penetration, 100 nm micelles demonstrated no improvement in therapeutic effect compared to 30 nm micelles despite carrying a larger payload.[11] It has long been postulated that strategies that could improve particle penetration will significantly improve tumor therapy.

Various approaches have been developed to improve nanoparticle penetration into tumors. Nanoparticles that become smaller in size[13,14] in response to pH and enzymes in the tumor microenvironment have been used to enhance diffusion into the interstitial space. Exogenous strategies including radiotherapy[15–18] and ultrasound[19] have also been used to increase particle accumulation and penetration by increasing tumor vascular permeability. Inflammatory modulators similarly increase vascular permeability,[20–22] while pharmacologic agents that disrupt the extracellular matrix (ECM)[23–28] or normalize the tumor vasculature[29,30] can directly reduce IFP, thereby improving nanoparticle penetration into tumors by restoring convective flow.[2] However, each of these methods has notable limitations. Particles that respond to the tumor microenvironment must be able to first detect these environmental signatures, which may be inaccessible (*e.g.* only present in the tumor core) or highly heterogeneous both within individual tumors and between patients. Environmental signatures present in the tumor can also be present at off-target sites.[31,32] Exogenous strategies relying on light and ultrasound energy sources that can be absorbed by the body may cause damage to adjacent and intervening tissues. Finally, pharmacological methods that rely on receptor binding may require precise dosing to achieve the desired effect while avoiding off-target effects,[31,32] or must be directly injected into the tumor[25,26] or into large arteries near the tumor site.[33,34]

Because biological tissues are essentially transparent to magnetic fields, magnetophoresis has been proposed as a bio-orthogonal means of increasing nanoparticle accumulation, and

potentially penetration, at tumor sites.[35–38] In this approach, magnetic drug carriers such as magnetoliposomes[39] or magnetic micelles[40] are injected intravenously, and a strong external magnet is used to localize the carriers to the tumor site. However, because magnetic fields from a single magnet are strongest at the surface of the magnet and rapidly fall off with distance, this strategy is limited to use in superficial tumors.[41] As a result, clinical trials using standard single-magnet devices to drive magnetophoresis for drug delivery have shown that this strategy is effective only when the tumor is < 5 mm from the magnet surface.[42–44] To target deep tissues, catheter-dependent magnetophoresis strategies have been developed, in which catheters are used to deliver nanoparticles to large arteries directly upstream of the tumor vasculature, and steering coils are then used to direct magnetic particle movement.[45,46] Though effective, these methods still require a catheter to be invasively maneuvered to the vicinity of the tumor.

To overcome these challenges, we have built a magnetic platform to improve the penetration of magnetic nanocarriers into solid tumors, regardless of their location, using a set of oppositely polarized external magnets (Fig. 1). A key innovation of this custom-built magnetic device is that the two oppositely polarized static magnets generate a sharp zero point at the center of the configuration. This zero point is surrounded by a strong and constant field gradient within the device. Since the magnetic force on magnetic particles is proportional to the magnetic field gradient when the magnetic moment is saturated,[47] the magnetic particles are driven radially outward from the zero point and into the tissue with uniform velocity throughout the device. In contrast, the velocity of a particle in a single magnet system drops off rapidly with distance from the magnet. With our approach, magnetophoresis is no longer limited to superficial tumors but can also be applied to tumors residing within deep tissues.

## RESULTS/DISCUSSION

### Superparamagnetic Iron Oxide Nanoparticle Micelle Characterization

Superparamagnetic iron oxide nanoparticle (SPION) micelles were synthesized by mixing ~10 nm SPIONs with the biodegradable amphiphilic diblock copolymer polyethylene glycol-*b*-polycaprolactone, PEG(4kDa)-PCL(3kDa) in toluene. This mixture was then added to water and sonicated, resulting in an oil-in-water emulsion. Following purification, the resulting micelles possess clusters of SPIONs entrapped within an ~85 nm diameter hydrophobic core (Fig. 2a) and have a hydrodynamic diameter in water of ~90 nm (Fig. 2b). The SPION micelles are extremely magnetic, with an r2 value of 544 $mM^{-1}s^{-1}$ at 1.41 T (60 MHz) (Fig. 2c). Additionally, the micelles are stable over 72 hours in FBS at 37°C, and for up to 1 month in PBS at 4°C (Fig. S1). Micelles were selected as the preferred platform for magnetophoresis, as opposed to individual SPIONs, because we presumed that hydrophobic drugs can be more readily loaded into micelles, in future therapeutic applications.

### Magnetic Device and Field Characterization

A custom magnetic device was designed and built using two 2” diameter (D) × 2” height (H) NdFeB rare earth element magnets (KJ Magnetics) with a surface field of 0.66 T. The magnets were oriented such that they were oppositely polarized, and placed in a guiding

aluminum tube (Speedy Metals). The tube included a window that allowed for the placement of samples or mice between the two magnets (Figs. 3a, S2). The device was designed such that the inter-magnet distance can be adjusted using a steel threaded rod (Fastenal). Rubber cylinders were placed between the magnets and the steel threaded rod to act as a cushion. Aluminum end plates (McMaster Carr) were used to constrain the maximum inter-magnet distance and act as a mechanical safety. (Figs. 3a, S2).

The magnetic field within the device was measured using a gaussmeter (AlphaLabs Inc). Measurements demonstrate the presence of a zero field region in both the axial (parallel to the configuration axis, Fig. 3b) and radial (perpendicular to the configuration axis, *i.e.* the plane equidistant between the magnets, Fig. 3c) directions, consistent with COMSOL simulations (Fig. 3d, e). A key feature of the magnetic configuration is that the field gradient $\nabla|B|$ is constant in both the axial (0.03 T/mm) and radial (0.015 T/mm) directions according to both simulations and experimental measurements (Fig. 3f). Therefore, unlike with single-magnet systems (Fig. S3), there is no drop-off in the field gradient with distance from the surface of the magnet in our device. Because magnetic force is proportional to gradient when the SPIONs are in their magnetically saturated regime (Fig. 4a), the constant gradient generates a constant force on the SPION micelles in most of the device, which translates to a constant velocity in viscous fluids like tissue (Fig. 4b).

## Demonstration of Magnetic Field Gradients Using Ferrofluid

To demonstrate that magnetic materials can be dispersed radially outward from the center of the device, ferrofluid (~20 mg/mL SPION micelles) was placed in a laser-machined (Universal Laser Systems) acrylic (McMaster) well plate. In the absence of any magnet, there is no applied field gradient to which the liquid in the wells responds (Fig. 5a, d). In the presence of a single magnet, as is typical of conventional magnetic targeting systems, the ferrofluid in the wells nearest the magnet moves towards the edge of the wells (Fig. 5b, e), while the ferrofluid in the wells furthest from the magnet is unaffected, due to the rapid drop-off in magnetic attractive forces with distance. This highlights one of the main limitations associated with single-magnet systems: even in a well plate with little resistance within the wells, only magnetic particles near the surface of the magnet will feel a magnetic force.

In contrast, when the well plate is placed in the magnetic device with oppositely polarized magnets, the ferrofluid in all wells moves outward towards the edge of the well away from the avoidance region at the center (Fig. 5c, f). Therefore, unlike single-magnet systems, our device generates magnetic field gradients that are not limited to locations near the magnet surface. These gradients can be harnessed to improve nanoparticle accumulation and penetration in deep tissues.

## Evaluation of SPION Micelles Movement in Agarose Phantoms

Next, we sought to understand the behavior of SPION micelles in porous materials, both to confirm that this behavior is consistent with theoretical predictions, and as a step towards understanding micelle behavior in tissues. To this end, 10 mg/mL SPION micelles were placed in a 0.4% agarose gel phantom. The phantom was exposed to three magnetic

configurations (no field/diffusion control, single magnet, and our device). In the absence of a magnetic field, SPION micelle movement was limited by diffusion, and little to no movement was detected over 24 hours (Fig. 6a, b). SPION micelles placed next to a single magnet moved slightly towards the direction of the magnet (Fig. 6a, c). SPION micelles placed in an agarose gel phantom in the device spread > 3.5 mm outward from the center in both directions (Fig. 6a, d). These results were consistent with simulations (Fig. S4), indicating that SPION micelle movement through the gel is well described by linear movement as a result of the uniform field gradient generated by the magnetic configuration in the device.

To quantify the improvement in SPION micelle movement through a 0.4% agarose gel phantom in the device compared to a diffusion control, we measured the distance that the leading edge of the SPION micelle profile had moved over time. By 24 hrs, the leading edge had moved > 10 times further in the magnetic device compared with diffusion. Moreover, the distance that the leading edge had moved increased linearly over time in the device, while the leading edge of the diffusion control moved as the square root of time, consistent with theoretical predictions (Fig. S5). Finally, as expected, SPION micelle movement through a 0.4% agarose gel phantom was dependent on size: above a cutoff size of ~110 nm, there was little to no micelle movement through the gel (Fig. S6).

## Magnetically-Enhanced Accumulation and Penetration of SPION Micelles in Tumors

To demonstrate that the magnetic device could improve SPION micelle accumulation and penetration into solid tumors, we intravenously injected SPION micelles into mice bearing syngeneic, orthotopic 4T1 breast tumors. Post-injection, the mice were either exposed to the device, a 1-magnet condition, or to no magnetic treatment (control). Magnetic exposure was broken into two 4-hour sessions separated by 12 hours of rest, for a cumulative total of 8 hours. MRI was performed pre-contrast and 24 hours post-contrast. Tumors showed T2 contrast enhancement in the control, 1-magnet, and treatment (device) groups (Fig. 7a, 7b, S7). This is consistent with previous observations, whereby even in the absence of active targeting, the EPR effect will encourage particle accumulation in solid tumors.[2,48] However, magnetic targeting using the device significantly enhanced particle accumulation compared to controls and the single magnet condition. In particular, post-contrast T2 images showed significant loss in signal (hypointensity) in the device-exposed mice compared to 1-magnet animals and unexposed controls (Fig. 7a, 7b, S7). These results indicate that the device is able to improve SPION micelle accumulation in the tumor beyond that achieved by EPR alone. Notably, there is no loss in signal in 1-magnet animals compared to unexposed controls, consistent with previous studies showing that magnetophoresis using a single magnet is distance-limited.[49]

To further assess the distribution and total accumulation of SPION micelles within the tumor, T2 maps[50] were created for each tumor pre- and post-contrast (Fig. 7c). The weighted means were then calculated from the pre- and post-contrast T2 maps in both device-exposed mice and control animals. The average reduction in the weighted mean between pre- and post-contrast T2 maps was 3.2 ms for the control group (Fig. 7c, S8a–c) and 2.1 ms for the 1-magnet group (Fig 7c, S8d–f) while the average reduction in the

weighted mean between pre- and post-contrast T2 maps was > 7.5 ms for the device-exposed groups (Fig. 7c, S8g–i). Measurements were made across 3 slices × 3 animals. The average reduction in the weighted mean for the treatment group was significantly greater than the control group ($p = 0.015$) and the 1-magnet group ($p = 0.046$) (Fig. 7d), further confirming higher SPION micelle accumulation.

## Histology

Gross examination of tumors excised from animals revealed that tumors from the device group were darker than the tumors excised from animals in the control group (Fig. 8a), indicative of higher concentrations of SPIONs, which are dark brown in color, within the tissue. To more closely evaluate the extent of SPION micelle accumulation in tumors, these tissues were sectioned, counterstained with eosin, and the SPIONs were stained with Prussian blue. Prussian blue staining demonstrated that control tumors had fewer particles and that the particles were closer to well-vascularized regions with red blood cells (Fig. 8b, c) compared to the device group (Fig. 8d, e). An analysis of 45 images (15 images × 3 tumors) for each group showed that in tumors of animals exposed to the device, 90% of particles were contained within 218 ± 17 μm (standard error (s.e.)) of the vasculature; that is, 10% of particles in the device-exposed tumors traveled further than 218 ± 17 μm (s.e.) from the vasculature. In contrast, in the control tumors, 90% of particles were found within 46 ± 5 μm (s.e.) of the vasculature ($p < 0.001$), and in the 1-magnet-exposed tumors, 90% of particles were found within 40 ± 3 μm (s.e.) of the vasculature ($p < 0.001$) (Fig. 8f). On average, particles in the device-exposed tumors traveled 96 ± 9 μm (s.e.) from the vasculature, while particles in the control tumors traveled 20 ± 2 μm (s.e) from the vasculature ($p < 0.001$) and particles in the 1-magnet-exposed tumors traveled 22 ± 2 μm (s.e.) from the vasculature ($p < 0.001$). Furthermore, based on the percent of pixels that were positive for Prussian blue, there were significantly more particles in the device group (0.011 ± 0.002% (s.e.) stained) compared to the control group (0.0034 ± 0.002% (s.e.) stained, $p = 0.0048$) and the 1-magnet group (0.0030 ± 0.001% (s.e.) stained, $p < 0.001$) (Fig. 8g).

Nanoparticle-based drug delivery to solid tumors is challenging due to the inability of nanoparticles to penetrate the tumor interstitium as a result of both physical and hydrostatic barriers.[5,51] While the pore size of the ECM is slightly greater than typical nanoparticle dimensions,[6,9] the increased IFP in tumors minimizes pressure-driven convective flow across the vascular epithelium.[2,7] As a result, nanoparticle penetration into tumors is often limited by diffusion out of the vasculature, which is consistent with the observation that small particles diffuse much more efficiently through the dense ECM than large particles.[7] For instance, Wang *et al.* found that 30 nm micelles are able to penetrate up to 100 μm into tumor tissues, while 100 nm micelles predominantly remain within 40 μm from blood vessels.[11] Similarly, Perrault *et al.* found that 100 nm particles are only able to diffuse within 20 μm of tumor vasculature.[4] To overcome this problem, various strategies have been developed to enhance nanocarrier penetration in tumors;[6,7,10,52] however, these are limited by the heterogeneity of the tumor environment and by potential off-target interactions with healthy tissue. As a result, magnetophoresis and magnetic drug targeting have become promising strategies for encouraging nanoparticle accumulation in tumors, with some magnetophoretic strategies having moved to clinical trials.[42–44] For instance, Lübbe *et al.*

used magnetic drug targeting to improve the accumulation of epirubicin-conjugated magnetic nanoparticles in patient sarcomas.[42–44] However, one of the primary challenges with magnetic targeting techniques is that they are limited to superficial tissues.[49] In this work, we have developed a magnetic targeting system based on a magnetic field with a zero point generated by two oppositely polarized cylindrical magnets. Because the field gradient in this type of configuration is linear throughout the device, it is possible to influence magnetic nanoparticles at any site in the body, including deep tissues.

We have shown that the magnetic platform described here is able to significantly improve tumor penetration of (~100 nm) magnetic nanocarriers. The top 10% of particles traveled ~5× further in the device-exposed tumors compared to the control tumors. Similarly, the average distance traveled by the particles was ~5× further in the device tumors compared to control tumors. There was also a > 3× increase in the total nanoparticle accumulation in the tumor, and a > 2× increase in T2 contrast in the tumor. Of note, because the surface of solid tumors tends to be more well-vascularized than the core,[53] even within device-exposed tumors, MRI images show nanoparticle deposition primarily at the tumor rim. Stronger magnetic fields (such as those generated by superconducting electromagnets) may improve nanoparticle deposition in the tumor core.

Nanoparticle locations within tumors were identified by positive Prussian blue staining. To quantify the distance that particles had penetrated into tissue, we calculated the distance between each nanoparticle and the edge of its nearest red blood cell. This method of quantifying nanoparticle extravasation from disorganized tumor vasculature is based on perfusion rather than structure. Therefore, we believe it is more representative of how far particles are able to travel through the interstitium while taking into account heterogeneous blood flow patterns in tumors.[54]

One limitation of the current prototype is that animals are exposed to the device for 8 hours under anesthesia to enhance particle penetration into tumors. A shorter treatment time would reduce the potential burden on both patients and providers for clinical development. Future work to replace the SPION particles with more magnetic formulations, including highly magnetic core-shell structures,[55] may mitigate this problem. Furthermore, the field gradient within the device can be increased by using electromagnetic systems or through the use of more than two magnets.[56,57] For instance, we estimate that using 9T superconducting electromagnets (as are used in current MRI systems) could increase the rate of particle movement and decrease the necessary treatment time by almost four-fold. These improvements would reduce the minimum device exposure time by increasing the force on the magnetic drug carrier. In addition to making improvements to the device, future studies will also validate the use of a multi-magnet device with deep-seeded orthotopic tumors, such as abdominal tumors, and focus on incorporating drugs into the micelle formulation for therapeutic uses of the system. Overall, we envision that this work sets the stage for the more effective use of magnetophoresis in the treatment of cancer.

## CONCLUSIONS

Drug delivery to solid tumors is often limited by nanoparticle penetration from the vasculature into tumor tissue. Magnetophoresis has been used to address this issue; however, current magnetophoresis methods are limited to use in surface tumors. Using a system of oppositely-polarized static magnets, we are able to achieve higher nanocarrier penetration and accumulation in deeper tumors.

## METHODS/EXPERIMENTAL

### SPION synthesis

To enhance the magnetic properties of the SPION-loaded micelles, cobalt-doped superparamagnetic iron oxide nanoparticles (SPIONs) were synthesized, as previously described.[58] The 10 nm cobalt-doped SPIONs could be readily synthesized in one step (*i.e.*, vs. sequential seed growth) and efficiently loaded into the micelles. Briefly, 1 mmol cobalt chloride (Alfa Aesar), 2 mmol iron (III) acetylacetonate (Sigma), 2 mmol oleic acid (Chem-Impex International), 6 mmol oleylamine (Sigma), and 5 mmol 1, 2-hexadecanediol (Sigma) were reacted in 20 mL benzyl ether (Sigma) in a two-neck flask while stirred under nitrogen. The reaction was heated to 200°C for 30 minutes, followed by heating to reflux for 75 minutes. The product was cooled to room temperature and washed with 100% ethanol by centrifugation at 5,500 g × 15 minutes. The pellet was resuspended in toluene and large aggregates were removed by centrifugation at 3,000 g × 15 minutes.

### Micelle synthesis and characterization

Micelles containing SPIONs were synthesized using a previously reported protocol.[59] Briefly, 4 mg Poly(ethylene oxide)-*b*-poly(ε-caprolactone) 4.0-*b*-3.0 (PEG-PCL 4k:3k) (Polymer Source), 0.4 mg PCL-5k, and 0.6 mg SPIONs were dissolved in 200 μL toluene. The solution was added to 4 mL of water and sonicated to form a homogeneous emulsion, and the toluene was allowed to evaporate at room temperature overnight to form micelles. The product was concentrated using a 100 kDa centrifugal filter (Millipore) and purified by centrifugation at 3,000 g × 10 minutes to remove large aggregates followed by centrifugation at 16,100 g × 10 minutes to remove empty micelles. Micelles were imaged by transmission electron microscopy (TEM) using a JEOL-1010 system and characterized by dynamic light scattering (Malvern). The micelles' magnetic properties were measured by NMR (Bruker).

### Simulation of micelle movement

First, to develop a theoretical basis for the behavior of SPION micelles in response to the magnetic device, we modeled particle movement through a porous phantom, composed of 0.4% agarose gel. Diffusion was modeled using a finite element model.

Magnetophoretic movement through the gel was modeled as a balance of the magnetic force $F_m = \nabla(\vec{m} \cdot \vec{B})$ and the drag force $F_d = -6\pi\eta r v$ where $m$ is the magnetic moment, $B$ is the magnetic field, $\eta$ is the viscosity of the medium (0.4% agarose gel, approximated as viscosity of water), $r$ is the radius of the particle, and $v$ is the velocity of the particle. Because the magnetic moment of the saturated particle[47,60] rotates to align with the

direction of the strong magnetic field, $F_d = \nabla(\vec{m} \cdot \vec{B}) = \nabla(mB) = m\nabla B$. Therefore, linear movement in combination with diffusion over time for particle $i$ was described by

$$x(i, t + \Delta t) = x(i, t) + p_{i,t} D\Delta t + \frac{2}{9\pi} \frac{m\nabla B}{r\eta} \Delta t$$

with $p_{i,t} = \pm 1$. The diffusion coefficient of nanoparticles in the gel was estimated at $10^{-6}$ $m^2 \cdot s^{-1}$ for the simulation. The initial positions of particles were a uniform distribution, and 10,000 particles were simulated.

## In Vivo tumor model and imaging

To grow a syngeneic, orthotopic tumor model, a 4T1 mouse mammary gland tumor cell line (ATCC) was cultured in DMEM at 37°C and 5% $CO_2$. Six-week old female Balb/c mice (Charles River) were injected with $10^6$ 4T1 cells in the mammary fat pad under the fourth nipple. After 7–10 days, the tumors reached a size of approximately 300 $mm^3$. Pre-contrast MRI was performed using a 4.7 T 50 cm horizontal bore MR system. SPION micelles were injected retro-orbitally at a concentration of 50 mg/kg. One-third of the animals were exposed to the magnetic device for 8 hours, while another third served as a no-magnet control, and the final third served as a single-magnet comparison. All mice exposed to the magnetic device were positioned on a custom acrylic bed, prior to being placed in the device, such that when the acrylic bed was placed within the magnetic device the zero point was located at approximately the center of the tumor. For single-magnet animals, the tumor was placed 10 mm away from the single magnet. Because the tumors have chaotically organized capillaries that run in various directions, there is no need to carefully arrange the magnetic field with respect to any particular blood vessel. Twenty-four hours after SPION micelle injection, post-contrast MRI was performed. Pre- and post-contrast images, including for T2 maps, were acquired using a gradient echo multi slice (GEMS) pulse sequence with TR = 1000 ms, TE = 6.3, 9.6, 12.9, 16.2, 19.5, 22.8, and 26.1 ms. The mice were sacrificed and the tumors were removed for histology. All animal protocols were approved by IACUC.

## Calculation of rSI, generation of T2 maps, and calculation of ΔT2

For quantification of nanoparticle accumulation based on MR images, regions of interest (ROIs) for tumor and water controls were selected by hand in ImageJ.

To determine the strength of T2 contrast in each tumor, the relative signal intensity (rSI) value was calculated by normalizing the average intensity of the tumor to the average intensity of a water control included with each image:

$$rSI = \frac{\sum_t I_t}{\sum_w I_w} \frac{A_w}{A_t}$$

where $A$ denotes area, $t$ denotes pixels in the tumor ROI, and $w$ denotes pixels in the water ROI. T2 maps were generated as previously described.[50] For each pixel ($i$, $j$) in the tumor ROI, T2 time was calculated by using Matlab to fit the curve

$$I_{ij} = C_{ij}e^{-TE/T2}$$

where $I_{ij}$ is the intensity of the pixel at $(i, j)$, $C_{ij}$ is a constant free parameter, $TE$ is the TE time in milliseconds at which the image was taken, and $T2$ is the constant free parameter of interest.

A weighted average was calculated as a representative measure of central tendency for the aggregate T2 value of each tumor. Briefly, the T2 values were separated into bins with edges in $E = \{0, 1, 2, \ldots, 100\}$. Each bin was assigned a value based on the frequency $f_i$ of T2 values in $[e_i, e_{i+1})$ such that $|F| = |E|-1$. The normalized frequency distribution N was calculated by taking

$$N = \frac{F}{\max(F)}$$

The weighted mean T2 value $\overline{T2}$ was calculated as

$$\overline{T2} = \frac{\sum_i e_i f_i}{\sum_i f_i} = \frac{\sum_i e_i n_i}{\sum_i n_i}$$

Finally, ΔT2 is calculated by subtracting $\overline{T2}$ of the post-contrast image from $\overline{T2}$ of the pre-contrast image for each slice.

Statistical significance levels were calculated using ANOVA.

## Histology

Tumors were harvested, fixed in 4% paraformaldehyde (Affymetrix) for 3 days, and dehydrated in 30% sucrose (Sigma) in PBS (Invitrogen) for 1 week. Tissues were then embedded in optimal cutting temperature (OCT) compound (Agar Scientific), sectioned into 10 μm slices, and thaw-mounted onto glass slides (Fisher). SPIONs were identified by Prussian blue staining for iron.[61] Briefly, sections were washed 3 × 5 min in water. Prussian blue reagent was made as a 1:1 (v:v) mixture of 2% potassium hexacyanoferrate (II) trihydrate (Sigma) and 2% hydrochloric acid (Fisher) in water. Sections were incubated in Prussian blue reagent for 30 min, followed by 3 washes with water. Sections were counterstained with eosin (Sigma) for 5 minutes, dehydrated in ethanol (50%, 70%, 90%, 100%), and cleared with xylene (Sigma). Finally, sections were coverslipped with DPX Mountant for histology (Sigma) and imaged under brightfield with an Olympus scope.

To determine the distance that nanoparticles had traveled from blood vessels, areas with high red blood cell densities were identified as blood vessels, and the distance between each Prussian blue-stained pixel and its nearest blood vessel was calculated. To quantify the amount of micelles that had accumulated in each, the percentage pixels stained with Prussian blue was calculated. Fifteen images were quantified for each tumor. Statistical significance levels were calculated using a ANOVA.

## Supplementary Material

Refer to Web version on PubMed Central for supplementary material.

## ACKNOWLEDGMENT

This work was supported by the NIH/NIBIB (R21 EB023989; DI), the NIH/NCI (R01 CA181429; AT), NIH/NINDS (T32 NS091006; JFL), and the U. of Penn. University Research Foundation Award (AT). We would like to acknowledge P. Rockett and B. Freedman for assistance with magnetic device construction, and S. Kartha for help with histology.

## REFERENCES

(1). Cooper GM The Development and Causes of Cancer In The Cell: A Molecular Approach; Sinauer Associates: Sunderland, MA, 2000.

(2). Danhier F; Feron O; Préat V To Exploit the Tumor Microenvironment: Passive and Active Tumor Targeting of Nanocarriers for Anti-Cancer Drug Delivery. J. Controlled Release 2010, 148, 135–146.

(3). Bae YH; Park K Targeted Drug Delivery to Tumors: Myths, Reality and Possibility. J. Controlled Release 2011, 153, 198–205.

(4). Perrault SD; Walkey C; Jennings T; Fischer HC; Chan WCW Mediating Tumor Targeting Efficiency of Nanoparticles Through Design. Nano Lett. 2009, 9, 1909–1915. [PubMed: 19344179]

(5). Baronzio G; Parmar G; Baronzio M Overview of Methods for Overcoming Hindrance to Drug Delivery to Tumors, with Special Attention to Tumor Interstitial Fluid. Front. Oncol 2015, 5, 165. [PubMed: 26258072]

(6). Barua S; Mitragotri S Challenges Associated with Penetration of Nanoparticles across Cell and Tissue Barriers: A Review of Current Status and Future Prospects. Nano Today 2014, 9, 223–243. [PubMed: 25132862]

(7). Jain RK; Stylianopoulos T Delivering Nanomedicine to Solid Tumors. Nat. Rev. Clin. Oncol 2010, 7, 653–664. [PubMed: 20838415]

(8). Heldin C-H; Rubin K; Pietras K; Östman A High Interstitial Fluid Pressure — An Obstacle in Cancer Therapy. Nat. Rev. Cancer 2004, 4, 806–813. [PubMed: 15510161]

(9). Yuan F; Dellian M; Fukumura D; Leunig M; Berk DA; Torchilin VP; Jain RK Vascular Permeability in a Human Tumor Xenograft: Molecular Size Dependence and Cutoff Size. Cancer Res. 1995, 55, 3752–3756. [PubMed: 7641188]

(10). Ruoslahti E; Bhatia SN; Sailor MJ Targeting of Drugs and Nanoparticles to Tumors. J. Cell Biol 2010, 188, 759–768. [PubMed: 20231381]

(11). Wang J; Mao W; Lock LL; Tang J; Sui M; Sun W; Cui H; Xu D; Shen Y The Role of Micelle Size in Tumor Accumulation, Penetration, and Treatment. ACS Nano 2015, 9, 7195–7206. [PubMed: 26149286]

(12). Huang K; Ma H; Liu J; Huo S; Kumar A; Wei T; Zhang X; Jin S; Gan Y; Wang PC; He S; Zhang X; Liang XJ Size-Dependent Localization and Penetration of Ultrasmall Gold Nanoparticles in Cancer Cells, Multicellular Spheroids, and Tumors *In Vivo*. ACS Nano 2012, 6, 4483–4493. [PubMed: 22540892]

(13). Wong C; Stylianopoulos T; Cui J; Martin J; Chauhan VP; Jiang W; Popovic Z; Jain RK; Bawendi MG; Fukumura D Multistage Nanoparticle Delivery System for Deep Penetration into Tumor Tissue. Proc. Natl. Acad. Sci. U. S. A 2011, 108, 2426–2431. [PubMed: 21245339]

(14). Ruan S; Cao X; Cun X; Hu G; Zhou Y; Zhang Y; Lu L; He Q; Gao H Matrix Metalloproteinase-Sensitive Size-Shrinkable Nanoparticles for Deep Tumor Penetration and PH Triggered Doxorubicin Release. Biomaterials 2015, 60, 100–110. [PubMed: 25988725]

(15). Lammers T; Peschke P; Kühnlein R; Subr V; Ulbrich K; Debus J; Huber P; Hennink W; Storm G Effect of Radiotherapy and Hyperthermia on the Tumor Accumulation of HPMA Copolymer-Based Drug Delivery Systems. J. Controlled Release 2007, 117, 333–341.

(16). Davies C. de L.; Lundstrøm LM; Frengen J; Eikenes L; Bruland S,ØS; Kaalhus O; Hjelstuen MHB; Brekken C Radiation Improves the Distribution and Uptake of Liposomal Doxorubicin (Caelyx) in Human Osteosarcoma Xenografts. Cancer Res. 2004, 64, 547–553. [PubMed: 14744768]

(17). Stapleton S; Milosevic M Radiation Effects on the Tumor Microenvironment: Implications for Nanomedicine Delivery. Adv. Drug Delivery Rev 2017, 109, 119–130.

(18). Li C; Ke S; Wu QP; Tansey W; Hunter N; Buchmiller LM; Milas L; Charnsangavej C; Wallace S Tumor Irradiation Enhances the Tumor-Specific Distribution of Poly(L-Glutamic Acid)-Conjugated Paclitaxel and Its Antitumor Efficacy. Clin. Cancer Res. 2000, 6, 2829–2834. [PubMed: 10914731]

(19). Mitragotri S Healing Sound: The Use of Ultrasound in Drug Delivery and Other Therapeutic Applications. Nat. Rev. Drug Discovery 2005, 4, 255–260. [PubMed: 15738980]

(20). Wu J; Akaike T; Maeda H Modulation of Enhanced Vascular Permeability in Tumors by a Bradykinin Antagonist, a Cyclooxygenase Inhibitor, and a Nitric Oxide Scavenger. Cancer Res. 1998, 58, 159–165. [PubMed: 9426072]

(21). Maeda H; Noguchi Y; Sato K; Akaike T Enhanced Vascular Permeability in Solid Tumor Is Mediated by Nitric Oxide and Inhibited by Both New Nitric Oxide Scavenger and Nitric Oxide Synthase Inhibitor. Jpn. J. Cancer Res 1994, 85, 331–334. [PubMed: 7515384]

(22). Fang J; Nakamura H; Maeda H The EPR Effect: Unique Features of Tumor Blood Vessels for Drug Delivery, Factors Involved, and Limitations and Augmentation of the Effect. Adv. Drug Delivery Rev 2011, 63, 136–151.

(23). Fan Y; Du W; He B; Fu F; Yuan L; Wu H; Dai W; Zhang H; Wang X; Wang J; Zhang X; Zhang Q The Reduction of Tumor Interstitial Fluid Pressure by Liposomal Imatinib and Its Effect on Combination Therapy with Liposomal Doxorubicin. Biomaterials 2013, 34, 2277–2288. [PubMed: 23290525]

(24). Pietras K; Rubin K; Sjöblom T; Buchdunger E; Sjöquist M; Heldin C-H; Stman A Inhibition of PDGF Receptor Signaling in Tumor Stroma Enhances Antitumor Effect of Chemotherapy. Cancer Res. 2002, 62, 5476–5484. [PubMed: 12359756]

(25). Eikenes L; Tari M; Tufto I; Bruland ØS; de Lange Davies C Hyaluronidase Induces a Transcapillary Pressure Gradient and Improves the Distribution and Uptake of Liposomal Doxorubicin (Caelyx™) in Human Osteosarcoma Xenografts. Br. J. Cancer 2005, 93, 81–88. [PubMed: 15942637]

(26). Zheng X; Goins BA; Cameron IL; Santoyo C; Bao A; Frohlich VC; Fullerton GD Ultrasound-Guided Intratumoral Administration of Collagenase-2 Improved Liposome Drug Accumulation in Solid Tumor Xenografts. Cancer Chemother. Pharmacol 2011, 67, 173–182. [PubMed: 20306263]

(27). Kato M; Hattori Y; Kubo M; Maitani Y Collagenase-1 Injection Improved Tumor Distribution and Gene Expression of Cationic Lipoplex. Int. J. Pharmacol 2012, 423, 428–434.

(28). Murty S; Gilliland T; Qiao P; Tabtieng T; Higbee E; Al Zaki A; Puré E; Tsourkas A Nanoparticles Functionalized with Collagenase Exhibit Improved Tumor Accumulation in a Murine Xenograft Model. Part. Part. Syst. Charact 2014, 31, 1307–1312. [PubMed: 26380538]

(29). Dickson PV; Hamner JB; Sims TL; Fraga CH; Ng CYC; Rajasekeran S; Hagedorn NL; McCarville MB; Stewart CF; Davidoff AM Bevacizumab-Induced Transient Remodeling of the Vasculature in Neuroblastoma Xenografts Results in Improved Delivery and Efficacy of Systemically Administered Chemotherapy. Clin. Cancer Res 2007, 13, 3942–3950. [PubMed: 17606728]

(30). Tong RT; Boucher Y; Kozin S V; Winkler, F.; Hicklin, D. J.; Jain, R. K. Vascular Normalization by Vascular Endothelial Growth Factor Receptor 2 Blockade Induces a Pressure Gradient Across the Vasculature and Improves Drug Penetration in Tumors. Cancer Res. 2004, 64, 3731–3736. [PubMed: 15172975]

(31). Muro S Challenges in Design and Characterization of Ligand-Targeted Drug Delivery Systems. J. Controlled Release 2012, 164, 125–137.

(32). Tredan O; Galmarini CM; Patel K; Tannock IF Drug Resistance and the Solid Tumor Microenvironment. JNCI, J. Natl. Cancer Inst 2007, 99, 1441–1454. [PubMed: 17895480]

(33). Nomura T; Inamura T; Black KL Intracarotid Infusion of Bradykinin Selectively Increases Blood-Tumor Permeability in 9L and C6 Brain Tumors. Brain Res. 1994, 659, 62–66. [PubMed: 7529648]

(34). Inamura T; Black KL Bradykinin Selectively Opens Blood-Tumor Barrier in Experimental Brain Tumors. J. Cereb. Blood Flow Metab. 1994, 14, 862–870. [PubMed: 8063881]

(35). Sun C; Lee JSH; Zhang M Magnetic Nanoparticles in MR Imaging and Drug Delivery. Adv. Drug Delivery Rev. 2008, 60, 1252–1265.

(36). Chertok B; David AE; Yang VC Polyethyleneimine-Modified Iron Oxide Nanoparticles for Brain Tumor Drug Delivery Using Magnetic Targeting and Intra-Carotid Administration. Biomaterials 2010, 31, 6317–6324. [PubMed: 20494439]

(37). Schleich N; Po C; Jacobs D; Ucakar B; Gallez B; Danhier F; Préat V Comparison of Active, Passive and Magnetic Targeting to Tumors of Multifunctional Paclitaxel/SPIO-Loaded Nanoparticles for Tumor Imaging and Therapy. J. Controlled Release 2014, 194, 82–91.

(38). Polyak B; Friedman G Magnetic Targeting for Site-Specific Drug Delivery: Applications and Clinical Potential. Expert Opin. Drug Delivery 2009, 6, 53–70.

(39). Fortin-Ripoche J-P; Martina MS; Gazeau F; Ménager C; Wilhelm C; Bacri J-C; Lesieur S; Clément O Magnetic Targeting of Magnetoliposomes to Solid Tumors with MR Imaging Monitoring in Mice: Feasibility. Radiology 2006, 239, 415–424. [PubMed: 16549622]

(40). Yang X; Chen Y; Yuan R; Chen G; Blanco E; Gao J; Shuai X Folate-Encoded and Fe3O4-Loaded Polymeric Micelles for Dual Targeting of Cancer Cells. Polymer (Guildf) 2008, 49, 3477–3485.

(41). Shapiro B; Kulkarni S; Nacev A; Muro S; Stepanov PY; Weinberg IN Open Challenges in Magnetic Drug Targeting. Wiley Interdiscip. Rev.: Nanomed. Nanobiotechnol 2015, 7, 446–457. [PubMed: 25377422]

(42). Alexiou C; Arnold W; Klein RJ; Parak FG; Hulin P; Bergemann C; Erhardt W; Wagenpfeil S; Lübbe AS Locoregional Cancer Treatment with Magnetic Drug Targeting. Cancer Res. 2000, 60, 6641–6648. [PubMed: 11118047]

(43). Lübbe AS; Alexiou C; Bergemann C Clinical Applications of Magnetic Drug Targeting. J. Surg. Res 2001, 95, 200–206. [PubMed: 11162046]

(44). Lübbe AS; Bergemann C; Riess H; Schriever F; Reichardt P; Possinger K; Matthias M; Dörken B; Herrmann F; Gürtler R; Hohenberger P; Haas N; Sohr R; Sander B; Lemke AJ; Ohlendorf D; Huhnt W; Huhn D Clinical Experiences with Magnetic Drug Targeting: A Phase I Study with 4'-Epidoxorubicin in 14 Patients with Advanced Solid Tumors. Cancer Res. 1996, 56, 4686–4693. [PubMed: 8840985]

(45). Pouponneau P; Leroux J-C; Soulez G; Gaboury L; Martel S Co-Encapsulation of Magnetic Nanoparticles and Doxorubicin into Biodegradable Microcarriers for Deep Tissue Targeting by Vascular MRI Navigation. Biomaterials 2011, 32, 3481–3486. [PubMed: 21315445]

(46). Pouponneau P; Leroux J-C; Martel S Magnetic Nanoparticles Encapsulated into Biodegradable Microparticles Steered with an Upgraded Magnetic Resonance Imaging System for Tumor Chemoembolization. Biomaterials 2009, 30, 6327–6332. [PubMed: 19695700]

(47). Shevkoplyas SS; Siegel AC; Westervelt RM; Prentiss MG; Whitesides GM The Force Acting on a Superparamagnetic Bead Due to an Applied Magnetic Field. Lab Chip 2007, 7, 1294. [PubMed: 17896013]

(48). Maeda H; Nakamura H; Fang J The EPR Effect for Macromolecular Drug Delivery to Solid Tumors: Improvement of Tumor Uptake, Lowering of Systemic Toxicity, and Distinct Tumor Imaging *In Vivo*. Adv. Drug Delivery Rev 2013, 65, 71–79.

(49). Rotariu O; Strachan NJC Modelling Magnetic Carrier Particle Targeting in the Tumor Microvasculature for Cancer Treatment. J. Magn. Magn. Mater 2005, 293, 639–646.

(50). Messroghli DR; Rudolph A; Abdel-Aty H; Wassmuth R; Kühne T; Dietz R; Schulz-Menger J An Open-Source Software Tool for the Generation of Relaxation Time Maps in Magnetic Resonance Imaging. BMC Med. Imaging 2010, 10, 16. [PubMed: 20673350]

(51). Sriraman SK; Aryasomayajula B; Torchilin VP Barriers to Drug Delivery in Solid Tumors. Tissue Barriers 2014, 2, e29528. [PubMed: 25068098]

(52). Fukumura D; Jain RK Tumor Microenvironment Abnormalities: Causes, Consequences, and Strategies to Normalize. J. Cell. Biochem 2007, 101, 937–949. [PubMed: 17171643]

(53). Soltani M; Chen P Effect of Tumor Shape and Size on Drug Delivery to Solid Tumors. J. Biol. Eng 2012, 6, 4. [PubMed: 22534172]

(54). Vaupel P; Kallinowski F; Okunieff P Blood Flow, Oxygen and Nutrient Supply, and Metabolic Microenvironment of Human Tumors: A Review. Cancer Res. 1989, 49, 6449–6465. [PubMed: 2684393]

(55). Kayal S; Ramanujan RV Anti-Cancer Drug Loaded Iron–Gold Core–Shell Nanoparticles (Fe@Au) for Magnetic Drug Targeting. J. Nanosci. Nanotechnol 2010, 10, 5527–5539. [PubMed: 21133071]

(56). Barnsley LC; Carugo D; Owen J; Stride E Halbach Arrays Consisting of Cubic Elements Optimised for High Field Gradients in Magnetic Drug Targeting Applications. Phys. Med. Biol 2015, 60, 8303–8327. [PubMed: 26458056]

(57). Voronin DV; Sindeeva OA; Kurochkin MA; Mayorova O; Fedosov IV; Semyachkina-Glushkovskaya O; Gorin DA; Tuchin VV; Sukhorukov GB *In Vitro* and *In Vivo* Visualization and Trapping of Fluorescent Magnetic Microcapsules in a Bloodstream. ACS Appl. Mater. Interfaces 2017, 9, 6885–6893. [PubMed: 28186726]

(58). Sun S; Zeng H; Robinson DB; Raoux S; Rice PM; Wang SX; Li G Monodisperse MFe2O4 (M = Fe, Co, Mn) Nanoparticles. J. Am. Chem. Soc 2004, 126, 273–279. [PubMed: 14709092]

(59). Al Zaki A; Joh D; Cheng Z; De Barros ALB; Kao G; Dorsey J; Tsourkas A Gold-Loaded Polymeric Micelles for Computed Tomography-Guided Radiation Therapy Treatment and Radiosensitization. ACS Nano 2014, 8, 104–112. [PubMed: 24377302]

(60). Chen R; Christiansen MG; Anikeeva P Maximizing Hysteretic Losses in Magnetic Ferrite Nanoparticles via Model-Driven Synthesis and Materials Optimization. ACS Nano 2013, 7, 8990–9000. [PubMed: 24016039]

(61). Thorek DLJ; Chen AK; Czupryna J; Tsourkas A Superparamagnetic Iron Oxide Nanoparticle Probes for Molecular Imaging. Ann. Biomed. Eng 2006, 34, 23–38. [PubMed: 16496086]

**SYNOPSIS.**

A system of oppositely polarized magnets encourages magnetic nanoparticle accumulation in solid tumors.

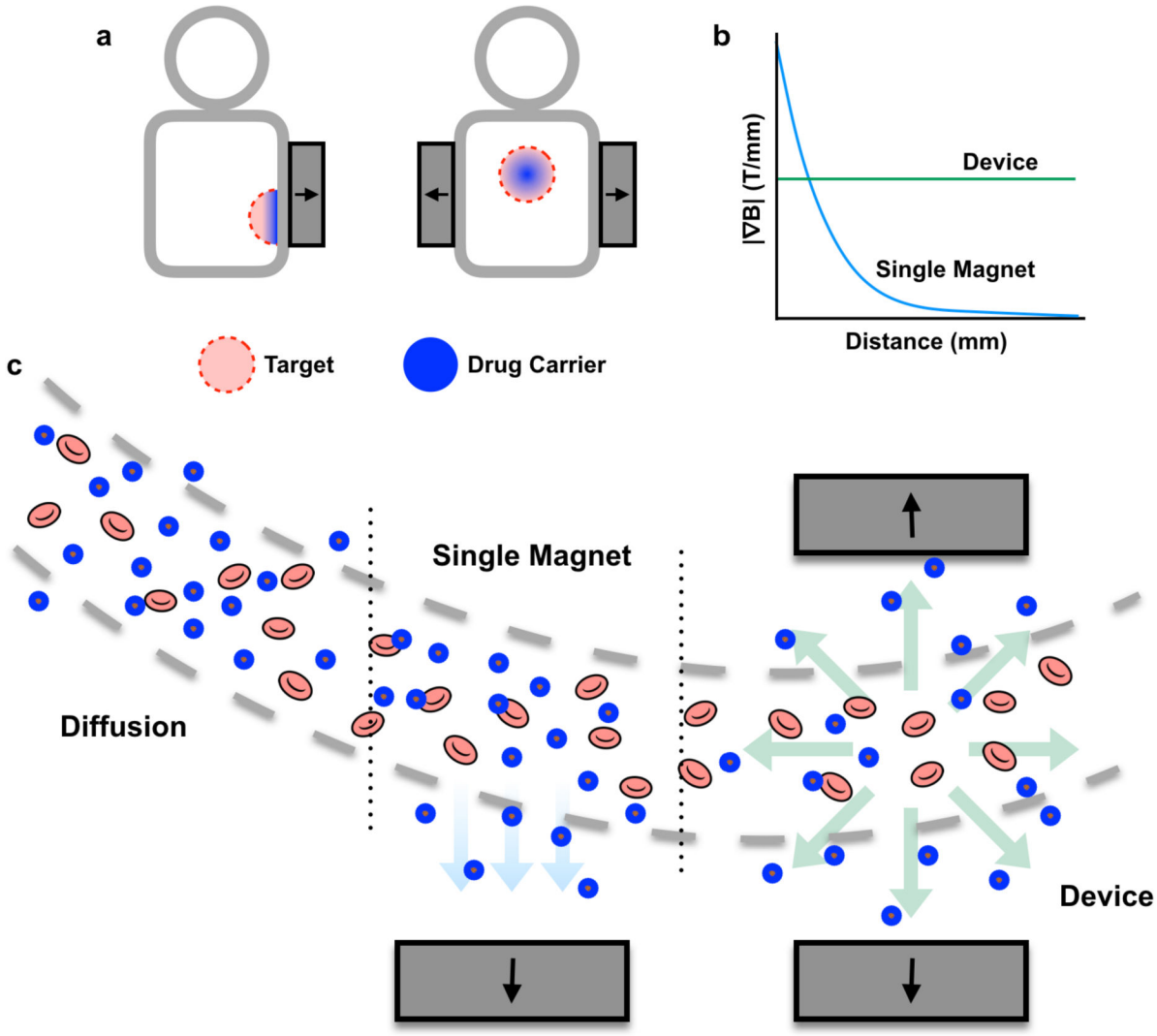


**Figure 1.**

A magnetic device, comprising two oppositely-polarized magnets, enhances magnetic drug targeting in deep tissues. (a) Magnetic targeting strategies that use a single external magnet are limited to use in surface regions. In contrast, this device can be used to encourage nanoparticle penetration into both deep and surface tissues. (b) While the gradient from a single magnet falls off rapidly with distance, the magnetic device generates a constant gradient throughout the tissue. (c) This constant gradient translates into a constant outward radial force on magnetic nanocarriers, encouraging nanocarrier penetration into tissues. In contrast, a single external magnet only pulls nanocarriers towards the direction of the magnet, while diffusion results in very little particle penetration into tissue compared to either magnetic strategy.

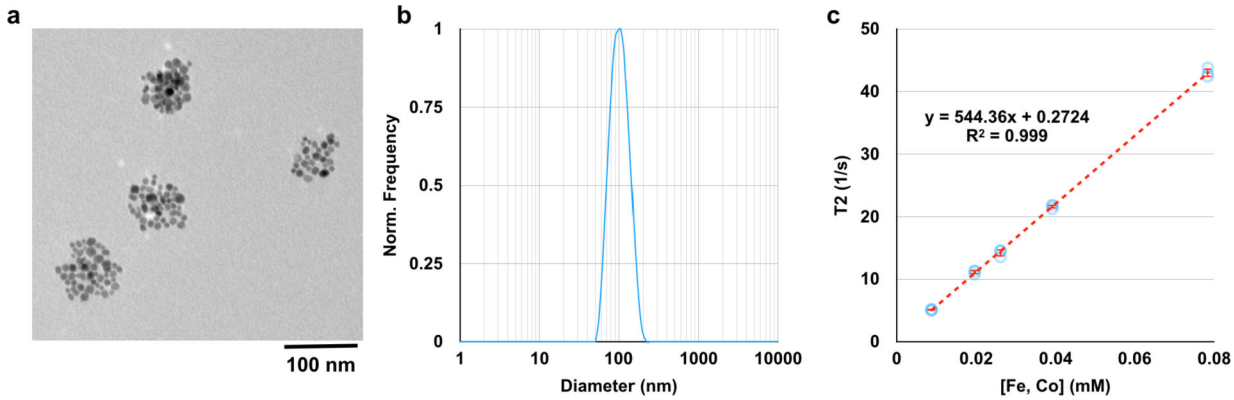


**Figure 2.**

SPION micelles are monodisperse and magnetic. (a) TEM image of SPION micelles shows a core size of ~85 nm, with each micelle core containing ~50 SPIONs. (b) In water, the micelles have a hydrodynamic diameter of ~100 nm (DLS by intensity). (c) SPION micelles have an r2 value of 544 ± 5 $mM^{-1}s^{-1}$.

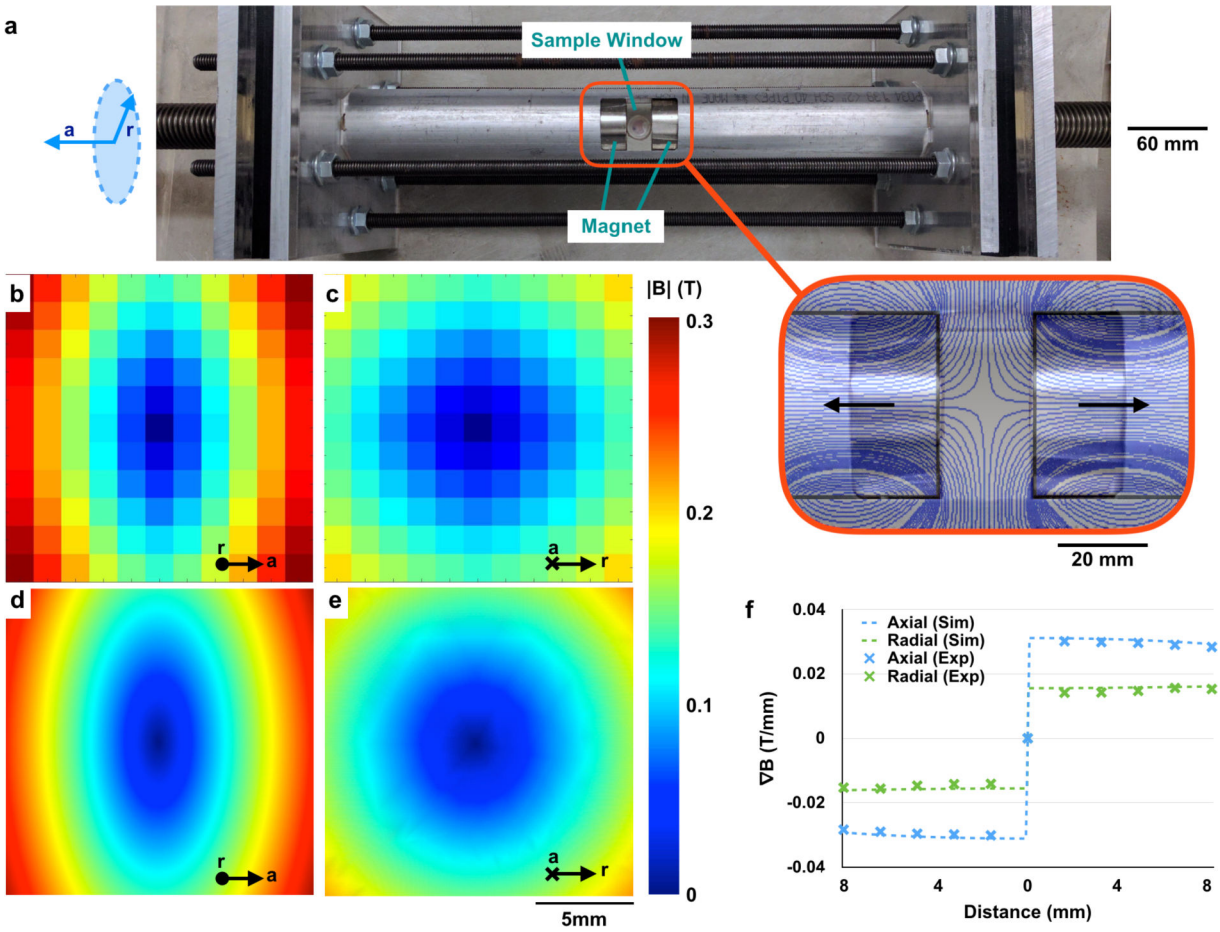


**Figure 3.**

The magnetic device contains a sharp zero point surrounded by constant field gradients. (a) The magnetic device comprises two oppositely-polarized static magnets aligned within an aluminum tube. Large steel threaded rods can be used to control the inter-magnet distance, while aluminum plates and steel rods mechanically stabilize the system. The magnet in the device's active region generates an avoidance region (outset) from which particles disperse. Measurements of the field within the active region show that this configuration results in a zero point at the center of the device in both the radial (b) and axial (c) directions, consistent with COMSOL simulations (d, e). The field gradient in the device is constant and directed radially outward (f). Inter-magnet distance for simulations and measurements = 20 mm.

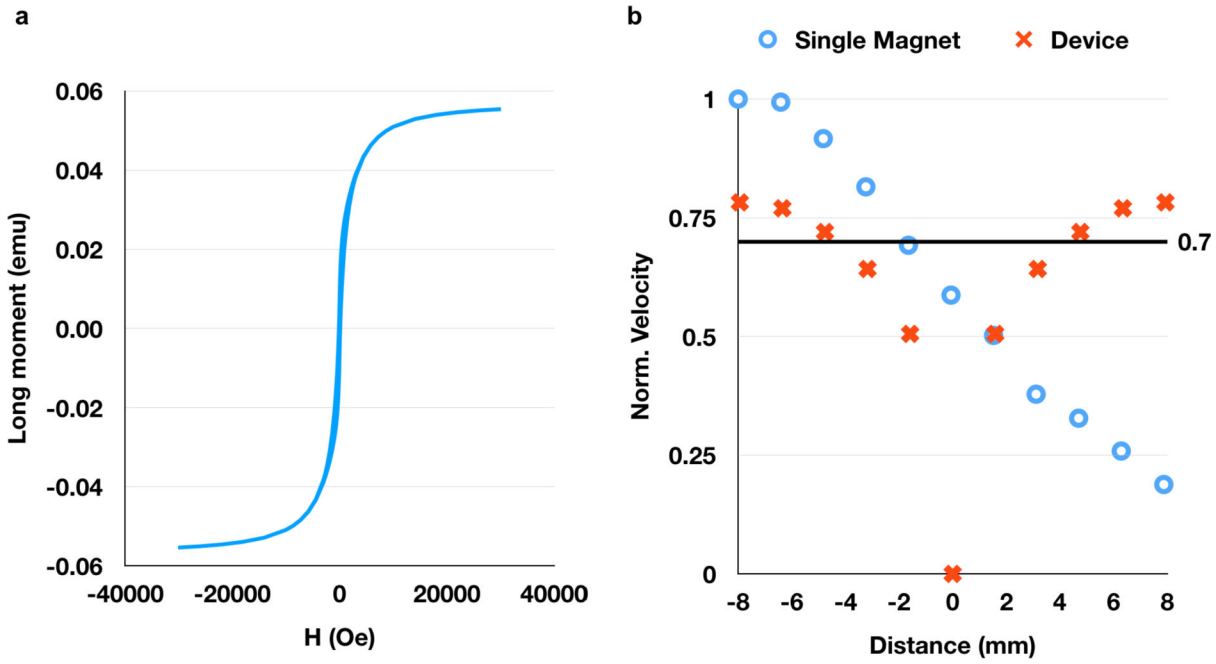


**Figure 4.**

The velocity of nanoparticles in the system depends on their magnetic moment (a) and the gradient of the magnetic field. In a single magnet system, the particle velocity (b) is high close to the magnet surface, but rapidly decreases to < 70% of the maximum velocity within 6 mm of the magnet surface. However, in our two-magnet system, all particles outside of a ~3 mm radius are expected to travel at > 70% of the maximum velocity achievable by a single magnet of the same strength, as calculated using the magnetic saturation curve (as shown in Fig. 4a) and the measured magnetic field (as shown in Fig. 3f) (b).

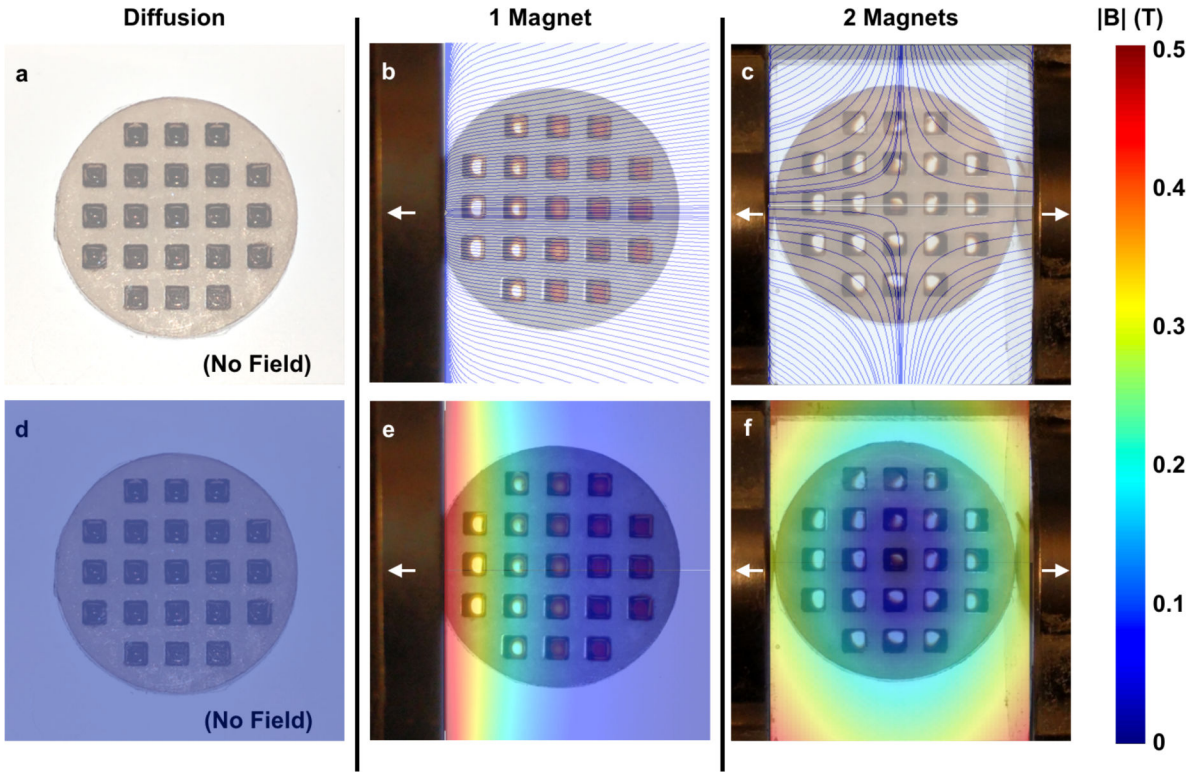


**Figure 5.**

Ferrofluids demonstrate the magnetic field and gradients within the device. In the absence of a magnetic field (diffusion only) the ferrofluid in the acrylic well plate does not respond (a, d). In the presence of a single magnet, the ferrofluid in the wells closest to the magnet respond, while the ferrofluid in further wells does not (b, e). In the magnetic device, ferrofluid in all wells move outward (c, f). Overlay: field lines (a-c), magnitude of magnetic field (d-f).

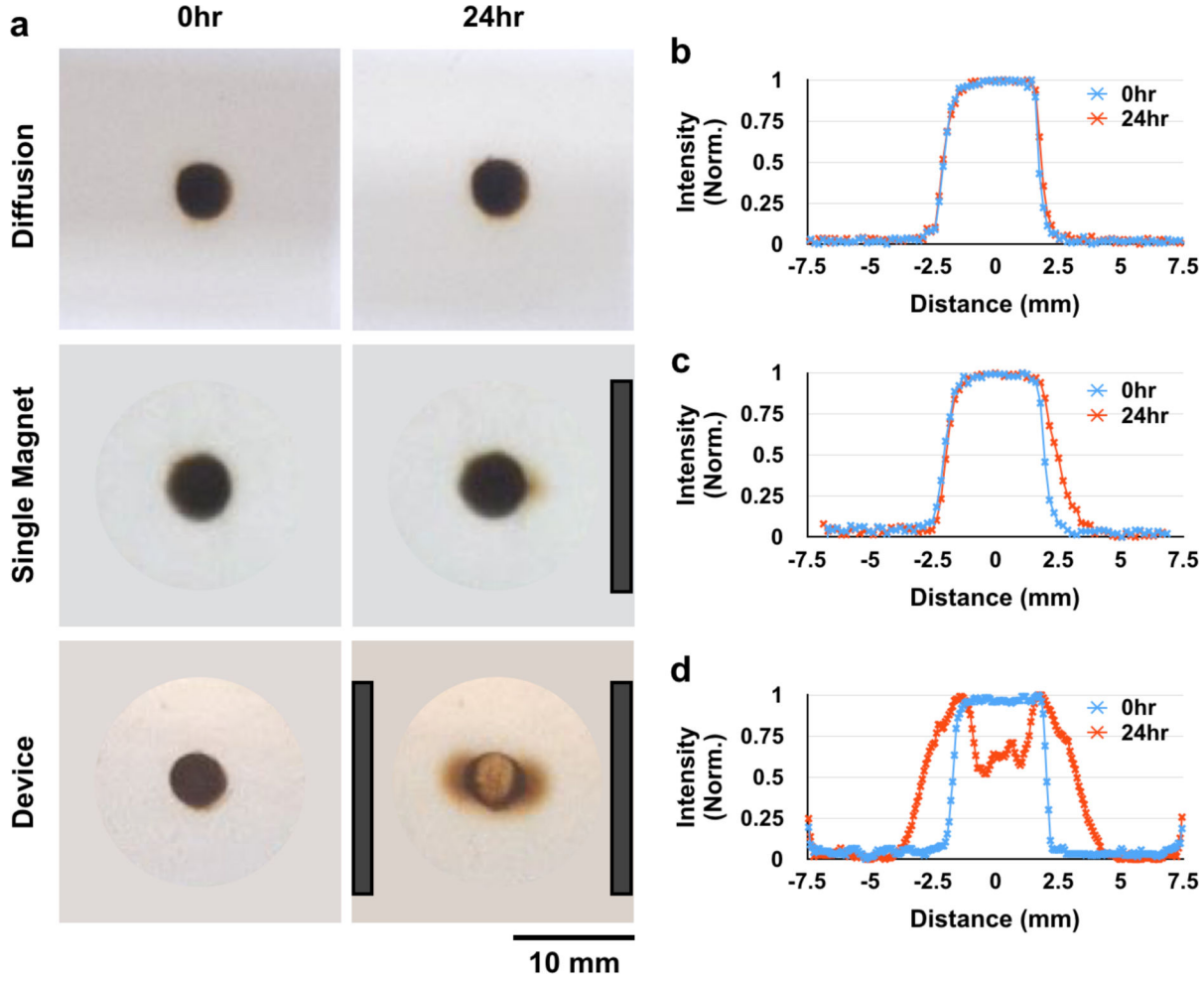


**Figure 6.**

The magnetic device radially disperses SPION micelles through a 0.4% agarose tissue phantom. There is minimal diffusion of SPION micelles through the tissue phantom over 24 hours (a: top, b). When placed next to a single magnet, SPION micelles move slightly through the gel toward the direction of the magnet (a: middle, c). However, in the magnetic device, particles disperse radially away from the zero point of the device (a: bottom, d). Magnet positions are indicated by dark gray bars.

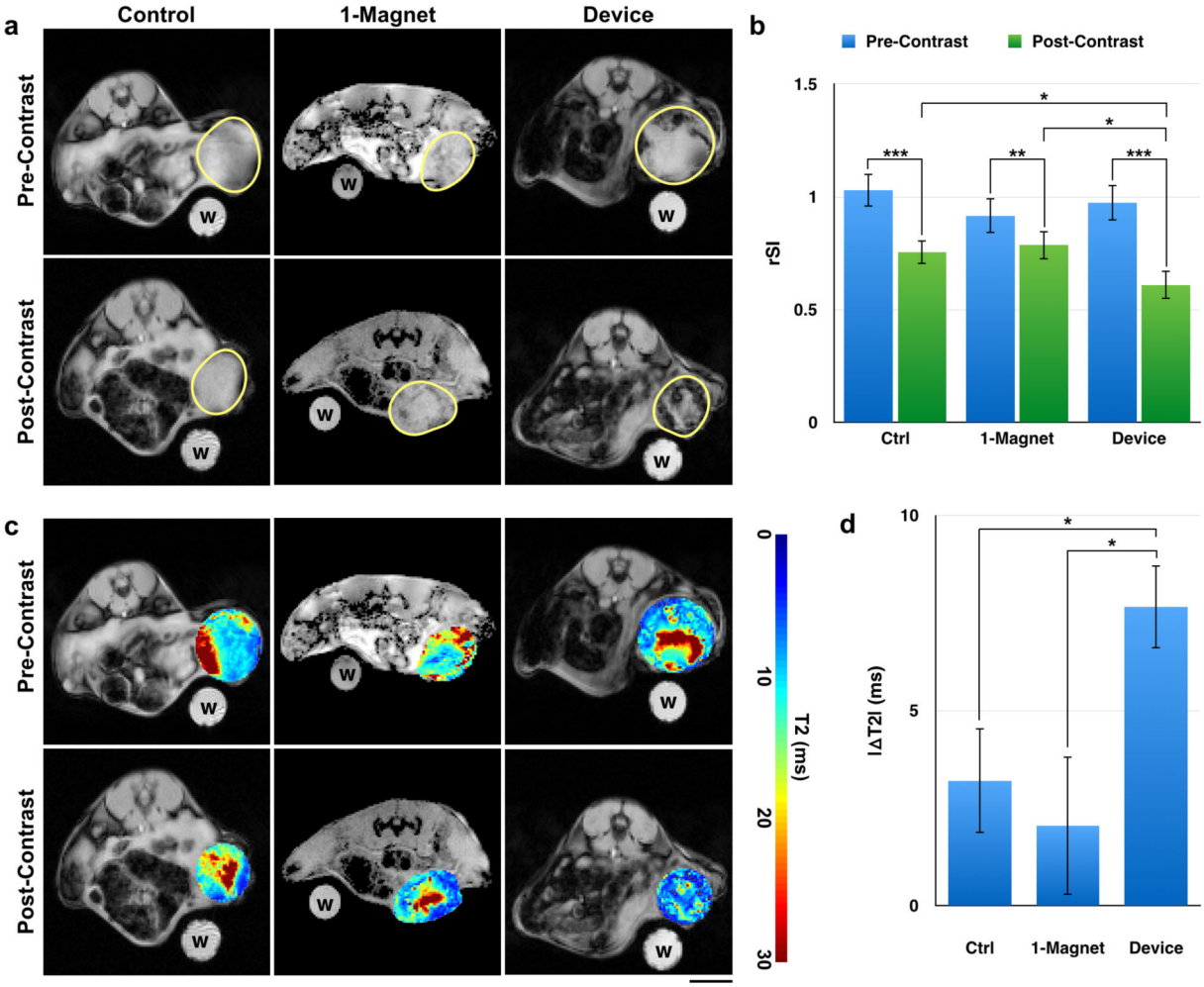


**Figure 7.**

The magnetic device significantly reduces T2 signal (hypointensity) from SPION micelles in tumors. (a) Pre- and post-contrast images have similar signal distributions in the control. However, mice that have been exposed to the device show much less T2 signal (hypointensity) post-contrast. Water control labeled “w”. Scale bar = 5 mm. (b) There is a significant reduction in average relative signal intensity (rSI) pre- and post-contrast in control ($p < 0.001$), 1-magnet ($p < 0.01$) and device-exposed ($p < 0.001$) animals, consistent with EPR. However, device animals also show a significant reduction in rSI compared to controls ($p = 0.037$) and 1-magnet-exposed ($p = 0.026$) animals post-contrast despite no difference in pre-contrast. There is no difference between control and 1-magnet rSI post-contrast. (c) T2 maps show the change in distribution of T2 times pre- and post-contrast for control and device animals. Tumors in device-exposed animals show more regions with shortened T2 times (indicating more accumulation of magnetic particles) compared to controls. (d) The change in the weighted average T2 time for each tumor slice was calculated. The shift in T2 time was significantly greater in device-exposed animals compared to control ($p = 0.015$) and 1-magnet-exposed ($p = 0.046$) animals. There is no difference between control and 1-magnet-exposed animals. N = 3 animals × 3 slices.

Statistical testing used ANOVA to establish a difference between distributions, followed by pairwise *t*-tests.

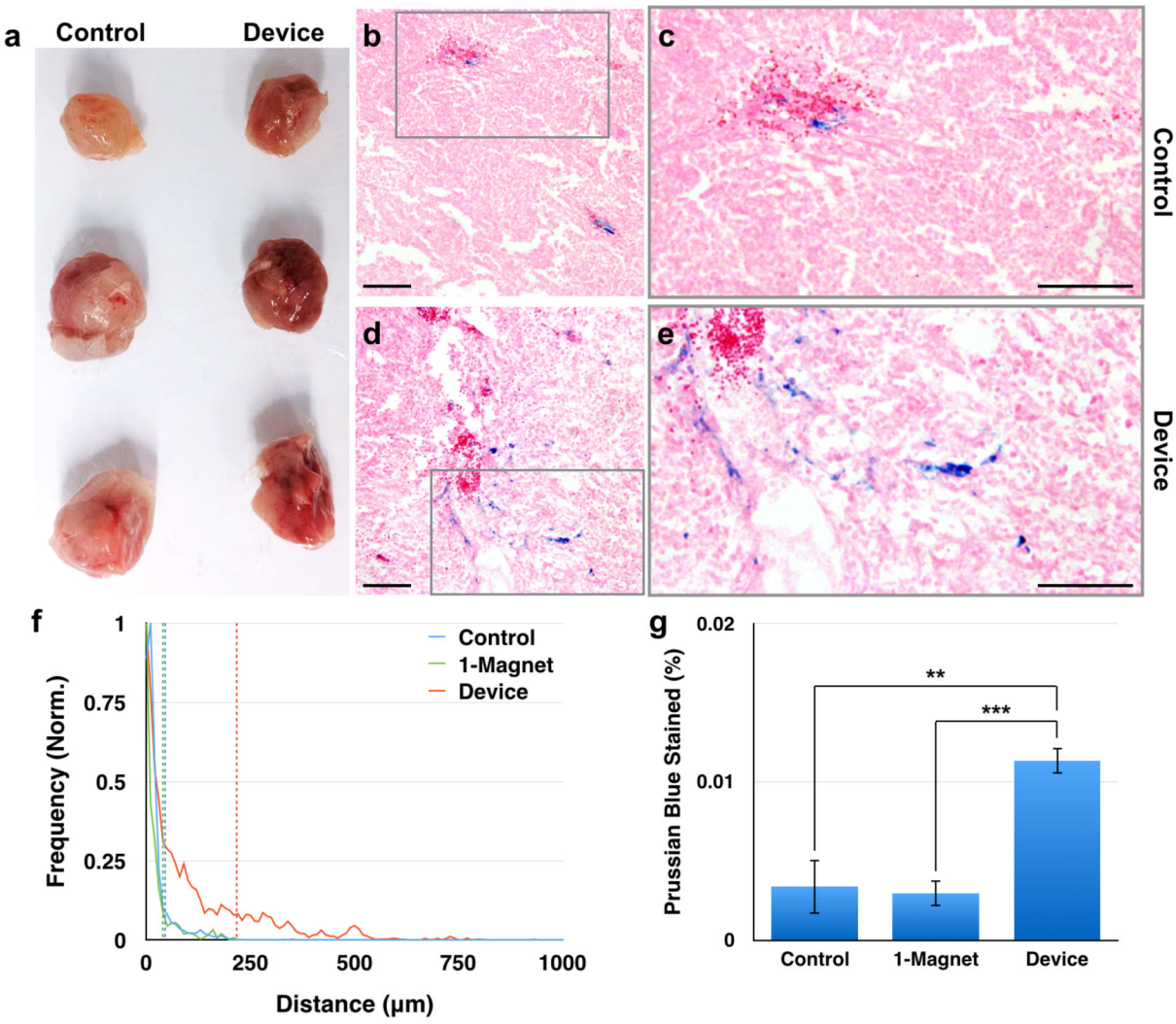


**Figure 8.**

Histology images show further tumor penetration by SPION micelles in device-exposed animals compared to controls. (a) Tumors harvested from device-exposed animals are grossly darker than those harvested from control animals. (b) Most nanoparticles, identified by Prussian blue staining, are located near vascular areas with red blood cells in controls (c: detail of gray box). (d) However, SPION micelles have dispersed from the vasculature and traversed through the tumor interstitium in device-exposed animals (e: detail of gray box). (f) SPION micelles are able to disperse significantly further from blood vessels in device-exposed animals compared to control animals ($p < 0.001$) and 1-magnet-exposed animals ($p < 0.001$). There is no difference between control and 1-magnet-exposed animals ($p = 0.36$). (g) Furthermore, there is more SPION micelle accumulation in device-exposed animals compared to control animals ($p < 0.001$) and 1-magnet-exposed animals ($p = 0.0048$). There is no difference between control and 1-magnet-exposed animals ($p = 0.81$) Scale bar in panels (b) – (e): 100 μm. N = 3 animals × 15 slices.